JOURNAL OF MATERIALS SCIENCE **39** (2004) 7023–7030

# The effect of grain boundary phase on contact damage resistance of alumina ceramics

JAE HUN KIM
*Department of Materials Science and Engineering, Korea Advanced Institute of Science and Technology, Yusong, Taejon 305-701, Korea; Agency for Defense Development, P.O. Box 35, Yusong, Taejon 305-600, Korea*

SHIWOO LEE
*Department of Materials Science and Engineering, Korea Advanced Institute of Science and Technology, Yusong, Taejon 305-701, Korea; Energy Materials Research Center, Korea Institute of Energy Research, Yusong, Taejon 305-343, Korea*

KEE SUNG LEE
*School of Mechanical and Automotive Engineering, Kookmin University, Seoul 136-702, Korea*

DO KYUNG KIM
*Department of Materials Science and Engineering, Korea Advanced Institute of Science and Technology, Yusong, Taejon 305-701, Korea*
*E-mail: dkkim@kaist.ac.kr*

The effect of grain boundary phase on contact damage behavior is investigated in alumina ceramics. Four types of aluminas doped with MgO, anorthite ($CaO{\cdot}Al_2O_3{\cdot}2SiO_2$), silica, and with both MgO and anorthite are prepared such that they have similar average grain size by adjusting sintering conditions. MgO-doped alumina composed of equiaxed grains shows brittle fracture behavior, and anorthite-doped alumina composed of elongated grains shows a quasi-plastic response under Hertzian sphere indentation. The co-doped alumina with MgO and anorthite, however, is damage tolerant even with its rounded grains, while silica-doped alumina with similar grain size and shape to anorthite-doped alumina shows abrupt strength degradation with low critical load for cone cracking. The damage behavior is discussed from the viewpoint of residual stress induced by thermal expansion mismatch between the grains and grain boundary phases. The damage tolerant behavior of alumina ceramics is significantly affected by the composition of grain boundary phase.


## 1. Introduction

Indentation methods have gained popularity as a simple and inexpensive technique for quantifying a wide range of mechanical properties of brittle ceramics and have been utilized in the analysis and characterization of fracture and deformation properties of brittle ceramics [1–4]. Hertzian indentation, in which a spherical indenter is used to apply concentrated stresses over a small area of the surface of a specimen surface, usefully simulates "blunt sphere" in service contact conditions [5]. Concentrated loads from contact with curved surfaces can be applied to ceramic components such as ceramic bearings, thermal barrier coatings, and biochemical structures. These stresses can induce localized damage, which can also degrade the strength of the components.

In polycrystalline ceramics, the fracture damage behavior and fracture toughness can be controlled by tailoring the microstructure and by grain bridging in the crack wake subsequent and pull-out, respectively [6]. Accordingly, studies of fracture damage behavior using toughness curves ($T$-curves) are essential to the understanding of grain-interlocking bridging in brittle ceramics. The microstructural features associated with long-crack toughness degrade short-crack properties such as strength, wear, and fatigue resistance. In other words, while materials composed of large grains with high aspect ratio and weak interface show rising $T$-curve behavior, they also have low resistance to wear and fatigue, because they provide easy fracture paths at large grain facets in residual tension. While long crack toughness has been increased by grain growth in alumina, it has been reported that strength and wear resistance has simultaneously been degraded [7, 8].

Recent studies of contact damage in tough ceramics have revealed that brittle to quasi-ductile transition by Hertzian indentation is influenced by changing from homogeneous to heterogeneous microstructure. Hertzian cone cracks are suppressed in these materials, and a

quasi-plastic deformation zone develops below the contact [3]. An irreversible deformation (quasi-plasticity) behavior beneath the contact was shown for heterogeneous microstructures featuring weak interfaces, large and elongated grains, and high internal stresses [9–11]. Damage is found to initiate in the subsurface region of high compression-shear beneath the contact, instead of in the surface region of weak tension outside the contact [1]. A shear fault deformation, specifically crystallographic twinning and slip in alumina, has been identified as the primary stage of damage in the heterogeneous microstructure [9]. Grain boundary microcracking at the ends of the constrained shear faults is known as the secondary stage. Comparative experiments on fine alumina ($\sim$2.5 $\mu$m) show no detectable microcracking, suggesting that average grain size plays a key role in the contact damage process. In contrast, the influences of elongated grains and the boundary phase composition of liquid-phase sintered (LPS) alumina ceramics are not well understood. The role of the intergranular boundary phase of LPS ceramics in considering the microstructural effects on the indentation behavior has not been reported.

In the present study, we investigate the role of the boundary phase composition on contact damage accumulation in LPS alumina ceramics. Four alumina ceramics with relatively coarse grains are prepared to demonstrate the effect of grain shape and boundary phase composition on the brittle-to-quasi-plastic transition. We controlled the aspect ratio of grains with MgO, and varied the grain boundary phase composition with $SiO_2$ and anorthite in the glassy phase.

## 2. Experimental

Four alumina ceramics were fabricated with various sintering additives. The alumina ceramics were designated as M (MgO), A (anorthite), S ($SiO_2$), and MA (MgO and anorthite), according to the sintering additives. Batches of powder were prepared by mixing alumina powder (AKP-50, Sumitomo, Tokyo, Japan) with the following sintering additives: Mg $(NO_3)_2{\cdot}6H_2O$ (Kokusan, Tokyo, Japan), TMOS (Tetra methyl ortho silicate, Aldrich, Milwaukee, USA), and Anorthite ($CaO{\cdot}Al_2O_3{\cdot}2SiO_2$). Anorthite was synthesized by heat treatment of $Ca(NO_3)_2{\cdot}6H_2O$ (Aldrich, Milwaukee, USA), $Al_2O_3$, and $SiO_2$ (High Purity Chemical Co., Saitama, Japan). Synthesized anorthite powder was pulverized in 2-propanol and toluene solvents in a vibration mill, and was sedimented to submicron particles for use as a sintering additive. Prepared powders were mixed to slurry in ethanol and milled for 24 h with zirconia balls in a polypropylene container. After drying, the softly agglomerated powder was crushed in an agate mortar and granulated. The powder mixtures were uniaxially compressed into disks, followed by cold-isostatic pressing at a pressure of 150 MPa. The green bodies were sintered at 1570 to 1620°C for 0.5 to 2.0 h in air.

The bulk density of the sintered materials was determined using Archimedes' principle. Surfaces of the sintered alumina specimens were polished to 1 $\mu$m finish, thermally etched, and examined by scanning electron microcopy (SEM). The SEM images were analyzed using an image analyzer for quantitative evaluation of the microstructure.

Hertzian indentations were made on the polished surfaces of the specimens using a tungsten carbide sphere with a radius $r = 3.18$ mm at a load up to $P = 2000$ N. The indentation damages were observed in Nomarski illumination of an optical microscope after gold coating. Bar specimens were indented in air at the center of the polished face at contact loads from $P = 0$ N to $P = 4000$ N or a Vickers indenter over a load range $P = 0.98$–$9.8$ N. Hertzian indentation 4-point flexural bending tests were conducted with a crosshead speed of 30 mm/min using a universal test machine. The failure origins of broken specimens were examined by optical microscopy. Disc samples with 3 mm of thickness were mechanically grinded to 50 $\mu$m thickness, ion-milled to perforations, and examined by transmission electron microscopy (TEM). TEM studies were performed at 200 kV of operating voltage (CM20, Philips, Eindhoven, Netherlands). The compositions of grain boundaries and intergranular boundary phases were analyzed by energy-dispersive spectroscopy (EDS).

## 3. Results

### 3.1. Microstructural features

The relative densities and average grain sizes of four aluminas, sintered with different additives, are summarized in Table I. All the specimens have densities over 96%, representing the highest value for MgO-doped (M-alumina). By varying the sintering conditions, the average grain sizes of all the specimens could be well controlled such that they were similar, thus eliminating the effect of average grain sizes. The representative microstructures of each specimen are shown in Fig. 1. As reported elsewhere [12], M-alumina is composed of equiaxed grains with a narrow distribution in sizes. On the contrary, anorthite-doped (A-alumina) and silica-doped (S-alumina) show bimodal microstructures, composed of small rounded grains and large plate-like grains. MA-alumina sintered with both MgO and anorthite shows microstructural features similar to those of M-alumina. This is consistent with the result that the microstructure of liquid phase sintered alumina varies with the addition of MgO [13]. Quantitative analysis of the distribution of aspect ratio for each grain, as shown in Fig. 2, confirms the microstructural features of each specimen: M-alumina and MA-alumina are mainly composed of grains with an aspect ratio under 2; A-alumina and S-alumina have many elongated grains with a high aspect ratio over 2.

TABLE I Relative densities and average grain sizes of four aluminas, sintered with different sintering additives

| Additives | MgO (500 ppm) | Anorthite (1 vol%) + MgO (500 ppm) | Anorthite (1 vol%) | $SiO_2$ (1 vol%) |
|---|---|---|---|---|
| Relative density (%) | 99.5 | 97.5 | 96.8 | 97.2 |
| Grain size ($\mu$m) | 5.3 | 5.9 | 5.6 | 6.0 |

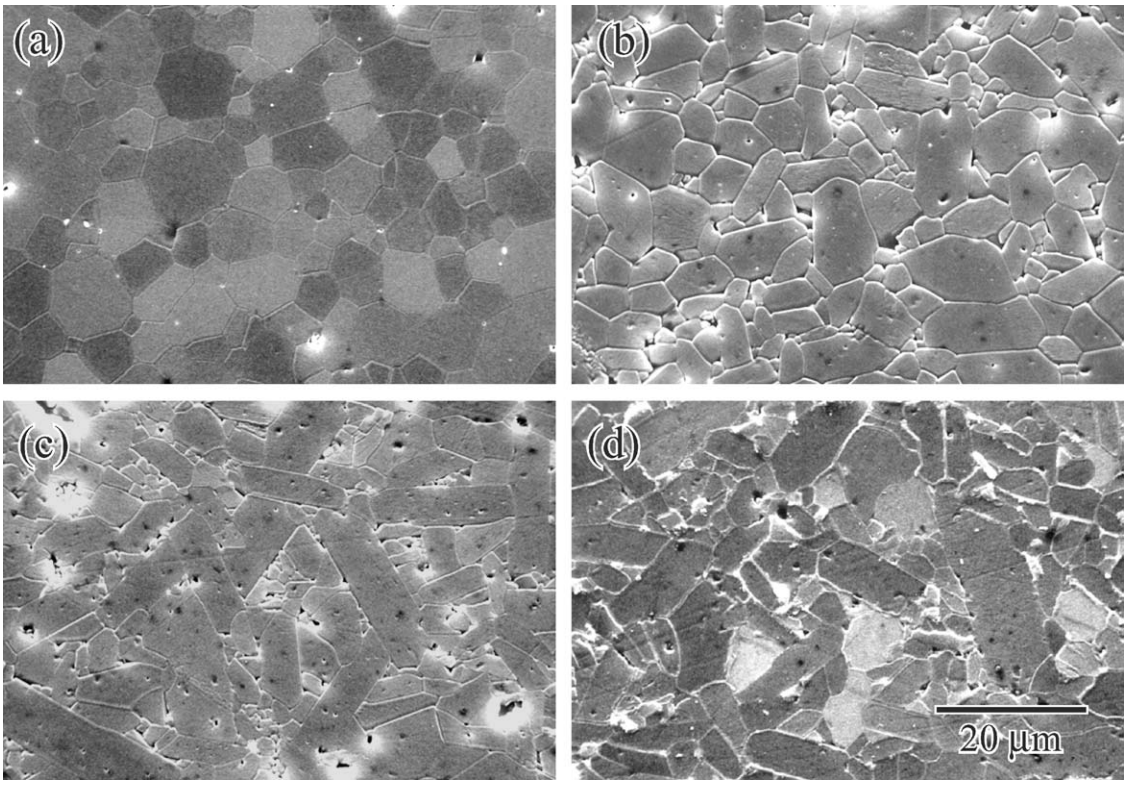


*Figure 1* SEM micrographs of aluminas sintered with (a) MgO, (b) anorthite + MgO, (c) anorthite, and (d) silica, respectively.

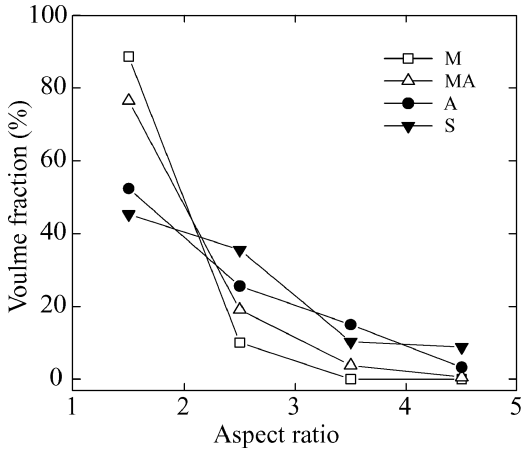


*Figure 2* Aspect ratio distribution of aluminas, sintered with MgO, anorthite, silica, and both MgO and anorthite.

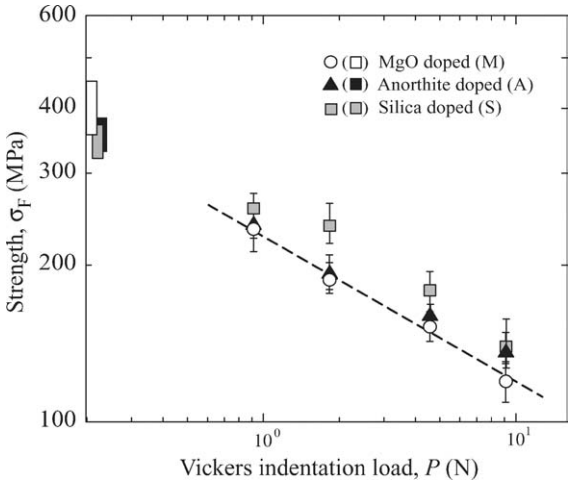


*Figure 3* Vickers indentation-strength curves of aluminas, sintered with MgO, anorthite, silica. The rectangles to the left denote failure from natural flaws.

### 3.2. Vickers indentation—strength test

The inert strength of M-alumina, 403 MPa, was higher than that of liquid phase sintered specimens, 345 MPa for A-alumina and 356 MPa for S-alumina, as shown in the rectangle at the left side in Fig. 3. The strength decreases with increasing Vickers indentation load, and the decrease is remarkable in the M-alumina. If a material has a single-valued toughness $T = T_o$, the applied stress $\sigma_A$ is related with the indentation load $P$ as follows [14]:

$$\sigma_A = \left(\frac{3T_o}{4\psi}\right)\left(\frac{T_o}{4\chi P}\right)^{1/3} \quad (1)$$

where $\psi$ is a geometrical coefficient that characterizes the penny-like crack configuration; $\chi$ is a coefficient that characterizes the intensity of the residual field in terms of indentation hardness $H$ and Young's modulus $E$. The existence of rising toughness curves ($T$-curves) may thus be inferred by departures from this relation. As the indentation-strength data of M-alumina follow the dotted-straight line fit of $(\text{slope})^{-1/3}$, the material can be regarded as having a single-valued toughness. In other words, the toughness of M-alumina has no dependence on crack size. On the other hand, it can be seen that there are some deviations from the straight line in A-alumina and S alumina. Thus liquid phase sintered aluminas are expected to have higher fracture toughness than M-alumina, showing

rising $T$-curve behavior. The deviation, however, is very small in comparison with that of other tough ceramics. While the grain morphology and the existence of liquid phase in the intergranular boundary has some effect on toughening behavior, it does not appear to be a strong factor.

### 3.3. Contact damage behavior

When a hard spherical indenter is pressed on the flat surface of a brittle material, a cone crack is produced from the vicinity of contact [15]. If the load reaches a critical value $P_c$, a surface ring crack initiates just outside the contact circle. As the load increases further, the ring crack propagates downward and flares outward into a truncated cone crack. On the contrary, Hertzian cone cracks tend to be suppressed in high-toughened ceramics; instead, a distributed deformed zone develops in a confined region beneath the contact area, consisting of an array of closed frictional shear faults with attendant "wing" microcracks at their ends. Weak grain boundaries in addition to large and elongated grains are required to induce occurrence of the damage zone. Subsurface damage becomes detectable at the critical $P_y$, at which the indentation stress-strain curve deviates from the linear relation of the indentation stress $p_o = P/\pi a^2$ ($P$ the load and $a$ contact radius) and strain $a/r$ ($r$ radius of spherical indenter). The critical load $P_c$ for cone crack initiation and $P_y$ for yield are summarized in Table II. M-alumina, sintered without liquid forming additives, has lower $P_c \sim$ 700 N than liquid phase sintered aluminas. While a typical surface ring crack develops in M-alumina at load $P = 700$ N, only an impression is observed under the same load in MA-alumina. Although MA-alumina contains a liquid forming phase, anorthite, the grains are equiaxed due to the presence of MgO [6]. Thus, it is assumed that the liquid phase in the intergranular boundary induces quasi-plasticity of equiaxed MA-alumina.

Although S-alumina and A-alumina both contain liquid phase sintering additives and their microstructures are very similar, they show different damage behavior. The critical load $P_c$ of S-alumina is lower than that of A-alumina and the yield stress is higher. On the other hand, MA-alumina and A-alumina, which might have similar grain boundary compositions but different microstructures, show analogous damage behavior. These results are discussed in the next section from the following viewpoints: (1) microstructural effects, and (2) grain boundary composition effects.

TABLE II The critical load for cone crack initiation $P_c$ and for yield $P_y$ of four aluminas, sintered with different sintering additives

| | MgO-doped (M) | MgO and Anorthite-doped (MA) | Anorthite-doped (A) | Silica-doped (S) |
|---|---|---|---|---|
| $P_y$(N) | – | 600 | 600 | 700 |
| $P_c$ (N) | 700 | 1000 | 1000 | 800 |

## 4. Discussion

### 4.1. Microstructural effect (Comparison between MA and A)

According to Table II, the critical loads $P_c$ and $P_y$ of MA-alumina are comparable to those of A-alumina, even though the grain morphologies of MA-alumina and A-alumina are dissimilar, as shown in Fig. 1. Photographs of surface damages in MA-alumina and A-alumina produced by a tungsten carbide sphere of radius $r = 3.18$ mm at loads $P = 800$–$1200$ N are shown in Fig. 4a and b. A slight deformation zone is observed at the surface of both materials indented at load $P = 800$ N, but no surface ring crack has initiated up to the load 1000 N. Fig. 5 shows the variation of fracture strength as a function of Hertzian indentation loads. Note that there is no strength loss in MA-alumina and A-alumina until the load is over 1500 N, which is higher than the critical load $P_c = 1000$ N. In general, an abrupt reduction in strength occurs near the critical load $P_c$ in brittle materials [6]. These results indicate that the fracture initiates not from surface cracks but from natural flaws, and that the surface crack has not fully developed downward to cone in MA-alumina and A-alumina. Surface micrographs of failure origins in MA-alumina and A-alumina broken in four-point flexure are shown in Fig. 6a and b. In these aluminas, the fracture originates closer to the contact center, traversing the contact peripheries almost orthogonally. This indicates failure from the microcrack region beneath the impression, not from the cone crack outside the contact area. The addition of a small amount of MgO to LPS alumina usually inhibits grain growth and stabilizes the microstructure, lowering the aspect ratio of grains [16]. It has been proposed that the additive operates by reducing the mobility of clean grain boundaries via a solid solution pinning mechanism, eventually suppressing the irregularity in growth rate between clean (unwet) boundaries and grain boundaries wetted by thin amorphous films [16]. Note that the contact damage behavior is not affected by the presence of a microstructural stabilizer, even though the addition of MgO to MA-alumina has induced microstructural features that are clearly different from those of A-alumina. These results imply that the existence of a liquid phase at grain boundaries has a greater effect on the damage behavior than microstructural features in these aluminas.

### 4.2. Effect of grain boundary composition (Comparison between A and S)

Surface views of contact damage in S-alumina, which has similar grain morphologies to A-alumina, are shown in Fig. 4c. While the surface ring crack is not clear even at a load $P = 1000$ N in A-alumina, a clear circle is formed at a lower load $P = 800$ N in S-alumina. This difference in damage behavior leads to a remarkable difference in the indentation-strength curves between A-alumina and S-alumina, as shown in Fig. 5. While there is no degradation of strengths until 1500 N in A-alumina, there are abrupt strength losses at load $P_c = 800$ N in S-alumina. A surface micrograph

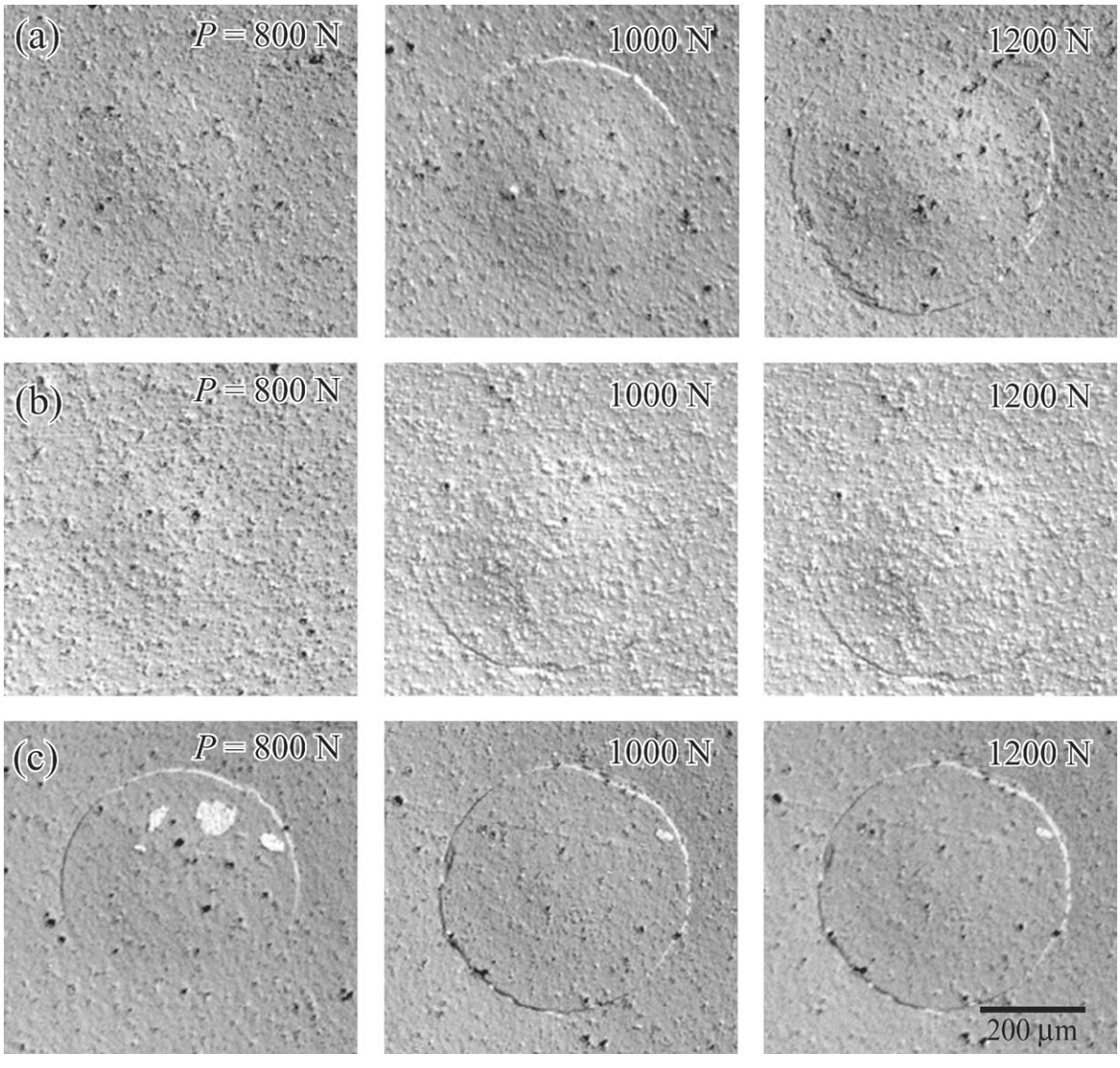


*Figure 4* Serial surface views of Hertzian contact damage in (a) MA, (b) A, and (c) S- alumina, respectively. The indentation was performed using WC sphere radius $r = 3.18$ mm and the indentation loads correspond to 800, 1000, and 1200 N from the top, respectively.

of failure origin in S-alumina (Fig. 6c) reveals that the fracture initiates from the base of the ring crack, indicating a failure from the cone crack below the contact.

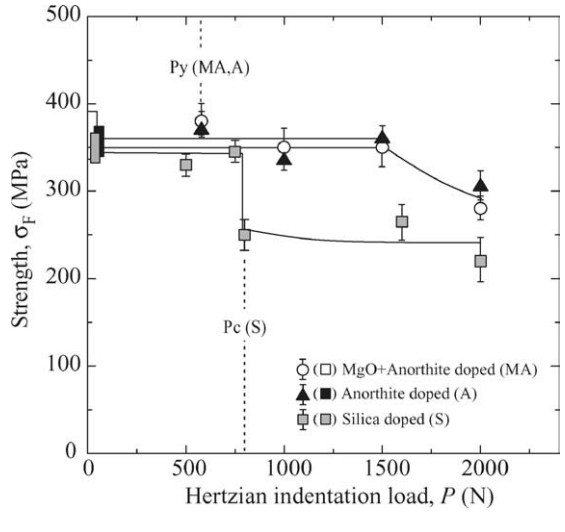


*Figure 5* Hertzian indentation-strength curves of aluminas, sintered with anorthite, silica, and with both MgO and anorthite. The rectangles to the left denote failure from natural flaws.

Note, while A-alumina shows quasi-plastic damage behavior, S-alumina shows brittle damage behavior. Although both have amorphous phases at grain boundaries and elongated grain morphologies, they show different damage behavior.

### 4.3. Grain boundary toughness

Harmer et al.'s hypothesis explains the microstructural discrepancies between A-alumina with elongated grains and MA-alumina with equiaxed grains [16]. MA-alumina and A-alumina, however, show similar quasi-plastic damage modes, even though they have different microstructural features. In contrast, S-alumina shows brittle damage mode even with elongated grains. These results reveal that grain morphologies have no major effect on indentation damage mode in these LPS aluminas. Moreover, although both A-alumina and S-alumina have liquid phases at grain boundaries, they show different damage modes. In Fig. 6b and c, while the fracture traverses the contact peripheries in A-alumina, indicating quasi-plastic damage mode, the failure occurs from a cone crack in S-alumina, indicating brittle damage mode. On a microscopic scale, the damage zone

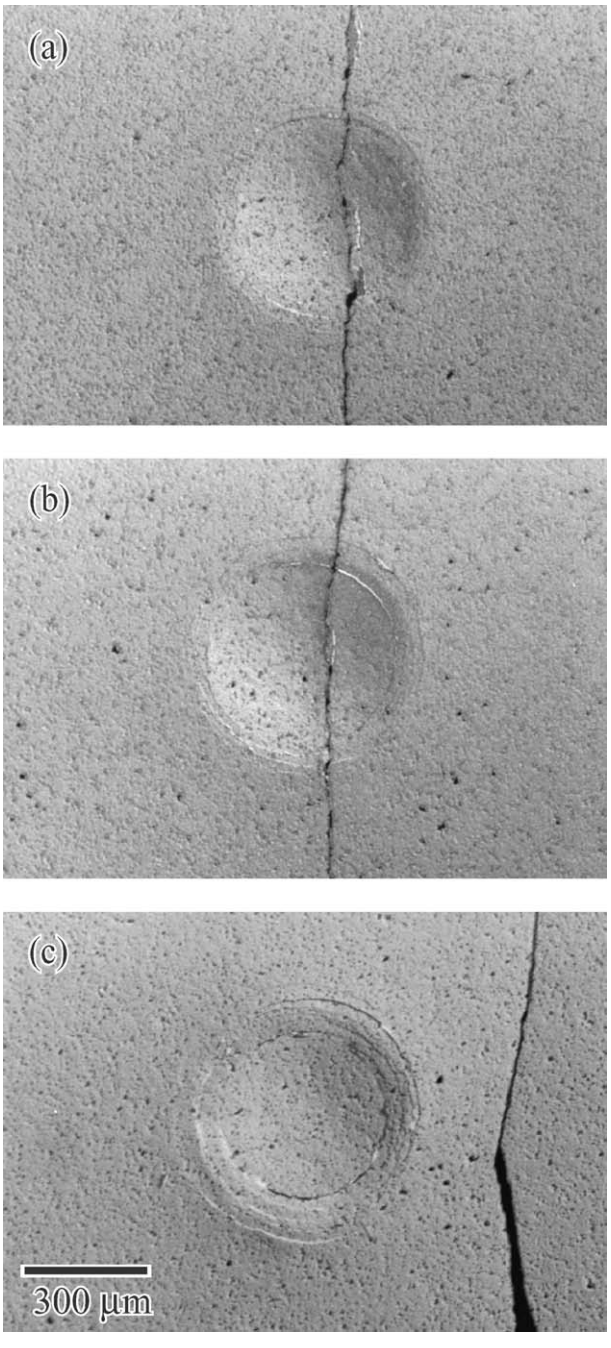


*Figure 6* Fracture origins of aluminas tested after the Hertzian indentation: (a) MA-alumina, (b) A-alumina, and (c) S-alumina.

that develops beneath the contact consists of microcracks that extend at shear faults. The shear faults in alumina are involved with the formation of twin or slip bands induced by shear stress [2]. The extent of microcrack opening depends on the 'weakness' of the grain boundaries. Residual stress, associated with the anisotropy of materials or differential expansion between the grain and grain boundaries, can be a source of grain boundary weakness [17–19]. Accordingly, the weakness of the boundaries can be inferred by measuring the thermal expansion mismatch between the grain and grain boundary phase in A-alumina and S-alumina.

It is assumed that the thin glassy phase, which has been known to wet grain boundaries in liquid phase sintered ceramics, would determine the microcrack opening behavior [20]. In the present study, we analyzed the glassy phase at triple grain junctions in LPS aluminas, because the glassy phase films at grain boundaries are usually too thin (typically a few nm) to be inspected. Fig. 7 presents TEM micrographs of triple grain junctions in A-alumina, MA-alumina, and S-alumina. TEM observation confirms that all LPS aluminas have faceted grain boundaries and glassy phase pockets at triple grain junctions, which usually means that the boundaries are wetted by liquid phase films. The glass compositions at the triple junctions, analyzed using EDS, are summarized in Table III. According to the literature [21, 22], the thermal expansion coefficient of pure $SiO_2$ glass is $5.5 \times 10^{-7}$/K, which decreases with increasing the amount of $Al_2O_3$ or decreasing that of CaO. Therefore, the grain boundary phase in S-alumina is expected to have a lower coefficient than that of pure silica glass because of the influence of $Al_2O_3$. Also, the coefficient of the grain boundary phase in A-alumina ($CaO{\cdot}Al_2O_3{\cdot}2SiO_2$) might be slightly lower than that of pure anorthite glass.

TABLE III EDS analysis results for the composition of grain boundary phase in MA-alumina, A-alumina, and S-alumina (in atomic %)

| Element specimen | Al | Si | Ca | Mg | Na | O |
|---|---|---|---|---|---|---|
| MgO + Anorthite | 13.09 | 29.82 | 2.80 | 0.39 | 0.45 | 53.45 |
| Anorthite ($CaO{\cdot}Al_2O_3{\cdot}2SiO_2$) | 11.98 | 20.67 | 0.95 | – | – | 66.40 |
| $SiO_2$ | 8.63 | 23.53 | – | – | – | 67.85 |

The residual stresses $\sigma$ induced by the thermal expansion mismatch between the grain and grain boundary phase can be calculated using the equation suggested by Evans *et al*. [19]:

$$\sigma_G = (\alpha_G - \alpha_g)\Delta T \times \left[\frac{1-2\nu_G}{E_G} + \frac{1+f_G+\nu(1-4f_G)}{2E_g(1-f_G)}\right]^{-1} \quad (2)$$

$$\sigma_g = -\frac{f_G}{1-f_G}\sigma_G \quad (3)$$

where, $\alpha$, $\nu$, $E$, and $f$ are the thermal expansion coefficient, Poisson's ratio, an elastic constant, and the volume fraction of grain ($G$) and grain boundary phase ($g$), respectively. The characteristic properties used in the calculation of residual stress are summarized in Table IV, and the residual tensile stress in alumina

TABLE IV The characteristic properties of $Al_2O_3$, anorthite and silica glasses

| | $E$ (GPa) | $\nu$ | $\alpha(\times 10^{-7}/^\circ C)$ $\perp_c$ | $\alpha(\times 10^{-7}/^\circ C)$ $\parallel c$ | Annealing point (°C) |
|---|---|---|---|---|---|
| $Al_2O_3$ grain | 393 | 0.2 | 86 | 96 | ~1600 |
| Anorthite glass | 89 | 0.3 | 42 | | 715 |
| Silica glass | 72 | 0.16 | 5.5 | | 1140 |

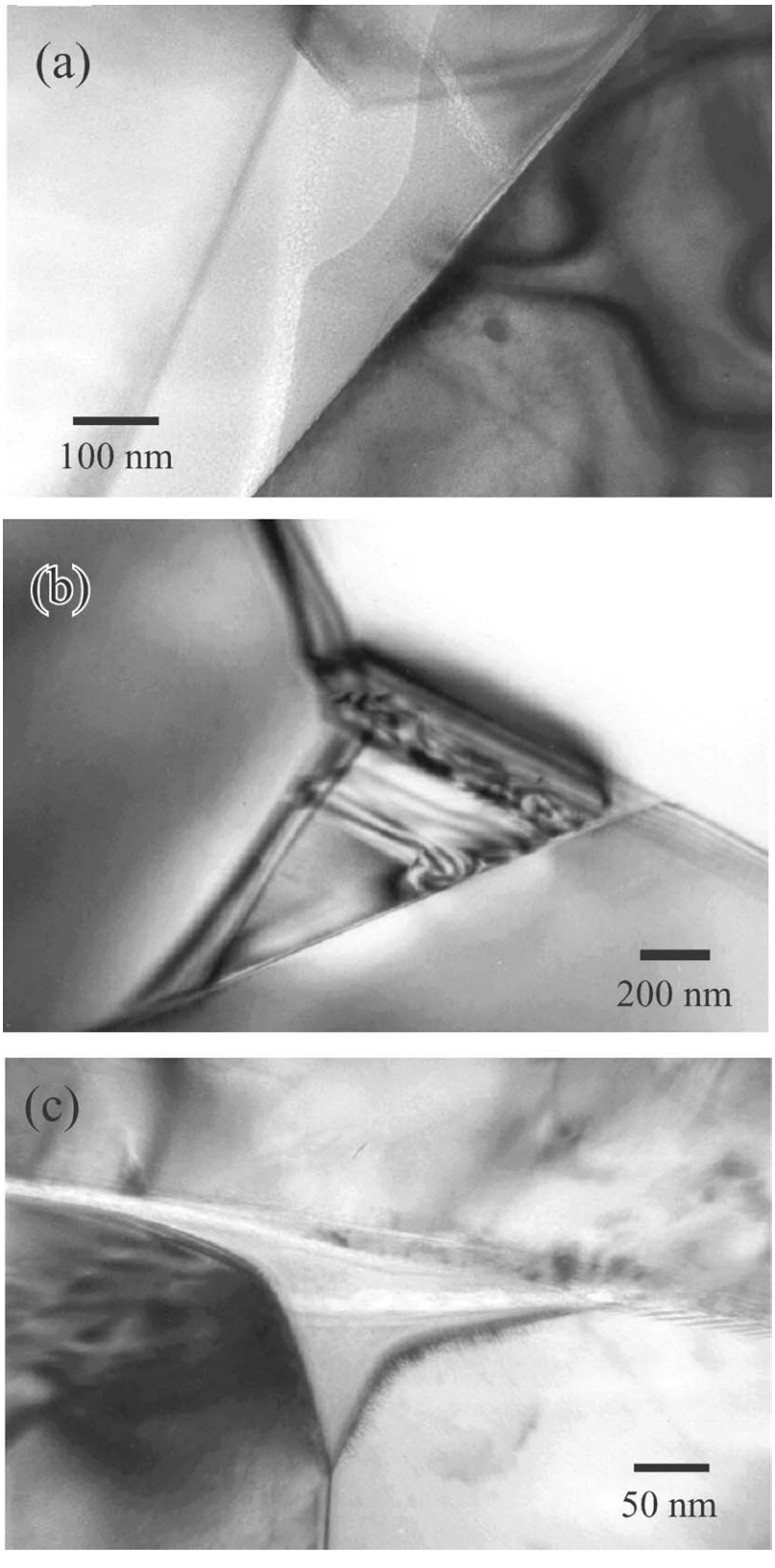


*Figure 7* TEM micrographs indicating glassy phases at the triple grain junction in (a) MA-alumina, (b) A-alumina, and (c) S-alumina.

grains and compressive stress in the grain boundary phase are indicated in Table V. The compressive stress on the grain boundaries is assumed to suppress the fracture resistance of the grain boundary and suppress microcrack opening. Note that the compressive stress in S-alumina (895 MPa) is greater than that in A-alumina (540 MPa). These results suggest that high compressive stress on the grain boundaries is responsible for the

TABLE V The calculated residual stresses induced by the thermal expansion mismatch between the grain and grain boundary phase

| | Residual stress (MPa) | |
|---|---|---|
| | A | S |
| $Al_2O_3$ grain | 5.4 | 9 |
| Grain boundary phase | −540 | −890 |

brittle damage behavior of S alumina. On the other hand, A-alumina and MA-alumina show similar damage behavior, even though the addition of MgO is effective in controlling the grain morphology. Therefore, the failure mode appears to be more sensitive to grain boundary toughness than grain morphology in the present study.

## 5. Conclusions

In the present study, we have investigated the role of grain boundary phase on contact damage accumulation in alumina ceramics, particularly liquid phase sintered aluminas with elongated microstructure, using Hertzian indentation tests. Four aluminas, including three LPS aluminas, are considered. M-alumina and MA-alumina are composed of relatively equiaxed grains, whereas A-alumina and S-aluminas are composed of large and elongated grains (Fig. 1). Although the microstructural features of MA-alumina are clearly distinguished from those of A-alumina by the addition of a small amount of MgO, the critical load for cone crack initiation $P_c$ and critical yield stress $P_y$ were almost coincident for these two aluminas (Table II). Similarity in damage behavior between MA-alumina and A-alumina is confirmed by four-point flexure tests after indentation and investigation of fracture origins (Figs 5 and 6). In contrast, S-alumina and A-alumina show different damage behavior, even though they have similar microstructural features. While S-alumina shows brittle damage behavior (low $P_c$ and significant strength degradation), A-alumina shows quasi-plastic damage behavior. These different damage behaviors are estimated by consideration of the residual stresses at the grain boundaries. The high compressive stress in the grain boundary phase is assumed to suppress microcrack opening and induce the brittle damage behavior of S-alumina. These results imply that the grain boundary phases may have a major effect on the damage behavior.


## Acknowledgements

This research was supported by a grant from the Center for Advanced Materials Processing (CAMP) of the 21st Century Frontier R&D Program funded by the Ministry of Science and Technology, Republic of Korea.


## References


1. F. GUIBERTEAU, N. P. PADTURE, H. CAI and B. R. LAWN, *Phil. Mag.* **68** (1993) 1003.
2. F. GUIBERTEAU, N. P. PADTURE and B. R. LAWN, *J. Amer. Ceram. Soc.* **77** (1994) 1825.
3. S. K. LEE, S. WUTTIPHAN and B. R. LAWN, *ibid.* **80** (1997) 2367.
4. D. K. KIM, Y.-G. JUNG, I. M. PETERSON and B. R. LAWN, *Acta Mater.* **47** (1999) 4711.
5. B. R. LAWN, "Fracture of Brittle Solids", 2nd ed., Cambridge Solid State Science Series, (Cambridge University Press, NY, 1993).
6. K. S. LEE, S. WUTTIPHAN, X.-Z. HU, S. K. LEE and B. R. LAWN, *J. Amer. Ceram. Soc.* **81** (1998) 571.
7. P. CHANTIKUL, S. J. BENNISON and B. R. LAWN, *ibid.* **73** (1990) 2419.
8. S. J. CHO, B. J. HOCKEY, B. R. LAWN and S. J. BENNISON, *ibid.* **72** (1989) 1249.
9. B. R. LAWN, N. P. PADTURE, F. GUIBERTEAU and H. CAI, *Acta Metall.* **42** (1994) 1683.
10. B. A. LATELLA, B. H. O'CONNOR, N. P. PADTURE and B. R. LAWN, *J. Amer. Ceram. Soc.* **80** (1997) 1027.
11. K. S. LEE, Y.-G. JUNG, I. M. PETERSON, B. R. LAWN and D. K. KIM, *ibid.* **83** (2000) 2252.
12. S. J. BENNISON and M. P. HARMER, *ibid.* **68** (1985) C22.
13. W. A. KAYSSER, M. SPRISSLER, C. H. HANDWERKER and J. E. BLENDELL, *ibid.* **70** (1987) 339.
14. L. M. BRAUN, S. J. BENNISON and B. R. LAWN, *ibid.* **75** (1992) 3049.
15. B. R. LAWN and T. R. WILSHAW, *J. Mater. Sci.* **10** (1975) 1049.
16. C. A. BATEMAN, S. J. BENNISON and M. P. HARMER, *J. Amer. Ceram. Soc.* **72** (1989) 1241.
17. S. J. BENNISON and B. R. LAWN, *Acta Metall.* **37** (1989) 2659.
18. P. F. BECHER, *J. Amer. Ceram. Soc.* **74** (1991) 255.
19. M. TAYA, S. HAYASHI, A. S. KOBAYASHI and H. S. YOON, *ibid.* **73** (1990) 1382.
20. P. F. BECHER, G. S. PAINTER, E. Y. SUN, C. H. HSUEH and M. J. LANCE, *Acta Mater.* **48** (2000) 4493.
21. E. B. SHAND, "Glass Engineering Handbook," (McGraw-Hill, 1958).
22. "Handbook of Glass Data," Part C: Ternary Silicated Glasses Elsevier, p. 755.



*Received 04 August 2003*
*and accepted 19 July 2004*